JMEPEG (2017) 26:5511–5518
DOI: 10.1007/s11665-017-2921-2

1059-9495/$19.00

Microstructure and Thermal Stability of A357 Alloy With and Without the Addition of Zr

Yu-Chih Tzeng, Vun-Shing Chengn, Jo-Kuang Nieh, Hui-Yun Bor, and Sheng-Long Lee

(Submitted January 2, 2017; in revised form July 27, 2017; published online October 3, 2017)

The principal purpose of this research was to evaluate the effects of Zr on the microstructure and thermal stability of an A357 alloy that has been subjected to an aging treatment (T6) and thermal exposure (250 °C). The results show that the addition of Zr had a significant influence on the refinement of the grain size, which enhanced the hardness and tensile strength of the A357 alloy under the T6 condition. During thermal exposure at 250 °C, the rodlike metastable β'-Mg_2Si precipitates transformed into coarse equilibrium phase β-Mg_2Si precipitates, resulting in a significant drop in the hardness and tensile strength of the T6 heat-treated A357 alloy. However, after thermal exposure, coherent, finely dispersed Al_3Zr precipitates were found to be formed in the T6 heat-treated A357 alloy. The addition of 0.1% Zr played a critical role in improving the high-temperature strength. Consequently, the A357 alloy with the addition of Zr demonstrated better mechanical properties at room temperature and high temperature than the alloy without Zr, in terms of both microstructure and thermal stability.

Keywords aluminum, heat treatment, microscopy, optical metallography

1. Introduction

The aluminum casting alloy A357 is a hypoeutectic Al-Si alloy that has been widely used for the fabrication of weight-sensitive components in industry because of its attractive comprehensive properties, such as castability, weldability, excellent specific strength and corrosion resistance (Ref 1). Iron is a common impurity in Al-Si alloys, where it readily forms intermetallic compounds with Al, eutectic Si and other elements (Ref 2). Under normal casting conditions, the formation of the acicular β-Al_5FeSi phase has deleterious effects on the ductility and toughness of the alloy. It is well accepted that the addition of Mn, Cr or Be can neutralize the embrittling effect of β-Al_5FeSi, by modifying the acicular shape into a less harmful, more compact form (Ref 3, 4). However, the strength of the A357 alloys is only effectively preserved at temperatures below 250 °C (Ref 5) because, above that temperature, the coarsening of the major strengthening β"-Mg_2Si and β'-Mg_2Si precipitates becomes unstable. They coarsen rapidly and then dissolve, causing a decrease in the performance of the alloy. This results in a reduction in the mechanical properties and limits high-temperature applications of this alloy for cylinder heads or engine components which require heat-resistant materials (Ref 6).

The element zirconium has the minimum diffusion flux of all the transition elements with aluminum (Ref 7), so the addition of Zr to aluminum-based alloys causes the precipitation of coherent metastable Al_3Zr precipitates with an ordered $L1_2$ structure, which hinders the movement of dislocations and increases the recrystallization temperature (Ref 8, 9). These metastable Al_3Zr precipitates have a strong resistance to dissolution and coarsening at high temperatures (Ref 10). They can also suppress the growth of the grain structure, thereby making it possible to increase the strength of the age-hardening condition of the T6 heat treatment during subsequent manufacturing operations, such as the hot rolling of wrought alloys (Ref 11, 12). There have been a few studies of the effect of Zr on cast Al-Si alloys (Ref 13-15). Raiszadeh (Ref 13) reported the formation of incoherent, coarse Al_3Zr particles in the microstructure during the solidification of an A356 alloy, causing grain refinement in the as-cast structure. Samuel et al. (Ref 15) showed that the addition of Ti, Zr and Ni to Al-Si-Cu-Mg alloys could improve their high-temperature strength. Although Zr enhances many aspects of the performance of wrought aluminum alloys, there has not been much in the way of discussion related to the effects of the addition of Zr on the mechanical properties of cast A357 alloys at high temperatures in the literature.

Therefore, in this work, both the microstructure and tensile properties of a A357 alloy after the addition of Zr are analyzed. The aim of this present study is to investigate the effect of the addition of trace amounts of Zr on the microstructure and high-temperature mechanical properties of the A357 alloys.

2. Materials and Methods

The experimental alloy was prepared in a 20 kg electrical resistance furnace by mixing Al-60 wt.% Ti, Al-10 wt.% Zr, Al-10 wt.% Sr master alloys and commercial purity Al

Yu-Chih Tzeng, Department of Power Vehicle and Systems Engineering, CCIT, National Defense University, Taoyuan, Taiwan; **Vun-Shing Chengn**, Optometry, College of Health Sciences, Central Taiwan University of Science and Technology, Taichung, Taiwan; **Jo-Kuang Nieh** and **Hui-Yun Bor**, Materials and Electro-Optics Research Division, National Chung-Shan Institute of Science and Technology, Taoyuan, Taiwan; and **Sheng-Long Lee**, Department of Mechanical Engineering, National Central University, Taoyuan, Taiwan. Contact e-mail: shenglon@cc.ncu.edu.tw.

(99.9 wt.%), Si and Mg to complete the targeted chemistry, with the different samples designated alloys A and B (Zr-containing), respectively. The alloy was melted at 760 °C under a protective atmosphere. The melts were degassed using pure Ar gas for 30 min and then poured into a preheated (400 °C) metallic mold with dimensions of 125 mm × 100 mm × 25 mm to complete the casting process. Table 1 presents the precise composition of alloys A and B (Zr-containing), determined using an optical emission spectrometer.

The T6 heat treatment was adopted for processing of the A357 alloy. According to the ASTM B917 standard, the specimens were solution-treated at 540 °C for 10 h and then water-quenched at room temperature, immediately followed by artificial aging at 160 °C for 6 h. In addition, a thermal exposure process involving heating of the T6 heat-treated alloys A and B (Zr-containing) to a constant temperature of 250 °C in an air furnace for 100 h was carried out. The mechanical properties were then tested at room temperature to assess the high-temperature performance of the alloys. In order to observe the grain structure, polished as-cast alloys A and B (Zr-containing) were etched in a 70% HCl, 25% HNO_3 and 5% HF solution for 10 seconds prior to being cleaned with deionized water. The test methodology for grain size measurement was the lineal intercept method. Each reported grain size measurement was an average of at least three separate measurements.

Metallographic observation of alloys A and B (Zr-containing) was carried out using a BX60 M optical microscope and a JEOL JXA-8500F electron probe microanalyzer, while an Oxford Inca energy-dispersive x-ray analysis spectroscope was used concurrently to perform composition analysis of the various intermetallic compounds. The metallographic specimens were cut transversely 200 mm from the bottom of the billets and then mounted, ground and polished down with 0.05-μm colloidal silica. TEM investigation was performed on a JEM-ARM200FTH electron transmission microscope to identify further detailed precipitates in the microstructures. A dual-beam focused ion beam (FIB, Versa 3D FEI) device was used to prepare the TEM specimens. The electrical conductivity measurements were determined as a percentage of the International Annealed Copper Standard (% IACS) using an Auto Sigma-2000 electrical conductivity meter.

Table 1 Chemical compositions of the studied A357 alloys (wt.%)

Alloy	Si	Mg	Fe	Sr	Zr	Ti	Al
A	6.87	0.61	0.10	0.015	N.D	0.11	Bal.
B	6.96	0.63	0.10	0.015	0.10	0.10	Bal.

N.D. non-detectable, *Bal* balance

A Rockwell hardness tester was used to measure the hardness of the T6 heat-treated alloys according to the ASTM E18 standard, at an applied load of 60 kg for 15 s. In addition, in order to test the thermal stability of the alloy, we also measured the hardness and tensile properties of the T6 heat-treated alloys after various aging heat treatment. Each reading was an average of five measurements. Specimens (Fig. 1) for tensile testing were machined from cast ingot sections about 10-15 mm away from the surface of the ingots, with a transverse orientation. Testing of the mechanical properties was conducted using the MTS-810 tensile tester and was performed according to ASTM E8 at a strain rate of 0.01 s^{-1}.

3. Results and Discussion

3.1 Characterization of Microstructure

Figure 2 shows images of the grain structure obtained after macro-etching of alloys A and B (Zr-containing) in the as-cast state. The average grain size of alloy A was determined to be 370 μm, with a standard deviation of 30 μm (Fig. 2a). However, the average grain size of alloy B (Zr-containing) was about 275 μm, with a standard deviation of 25 μm, indicating significant grain refinement following the addition of Zr (Fig. 2b).

Figure 3(a) shows optical micrographs of as-cast alloy A without the addition of Zr with fibrous eutectic Si, Mg_2Si and nodular iron-bearing phases distributed throughout the inter-dendritic regions. In addition to the fibrous eutectic Si, Mg_2Si and nodular iron-bearing phases, acicular or platelike iron-bearing phases can be observed in the as-cast alloy B (Zr-containing), as shown in Fig. 3(b). EPMA micrographs of the intermetallic compounds in as-cast alloys A and B (Zr-containing) are shown in Fig. 4. The results of composition analysis of the intermetallic compounds marked by the white arrows and letters in Fig. 4 are tabulated in Table 2. The presence of an iron-bearing phase was detected in the microstructure of as-cast alloy A, as shown in Fig. 4(a). EPMA analysis revealed that the $Al_7Si_2Fe_3$ intermetallic compound contained 63.5 wt.% Al, 9.1 wt.% Si and 27.2 wt.% Fe (Table 2). The intermetallic compounds in as-cast alloy B (Zr-containing) shown in Fig. 4(b) are confirmed to have not only a $Al_7Si_2Fe_3$ phase but also a platelike $(Al,Si)_3(Ti,Zr)$ phase.

3.2 TEM Analysis

The precipitation sequence for as-cast Al-Si-Mg alloys starts with the precipitation of GP zones. The GP zones elongate and grow into a needle-shaped coherent β”-Mg_2Si phase. Increasing

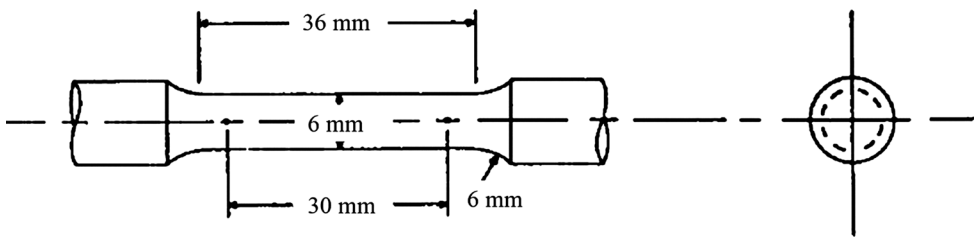

Fig. 1 Schematic representation of the standard tensile specimen

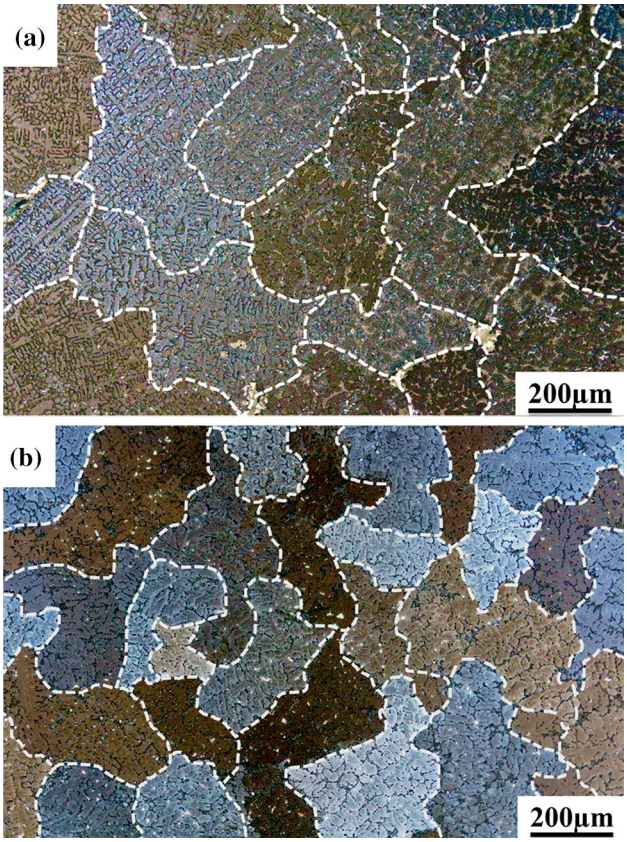

Fig. 2 Grain structure of the as-cast A357 alloys, showing the effect of the Zr addition: (a) alloy A (Zr-free) and (b) alloy B (Zr-containing)

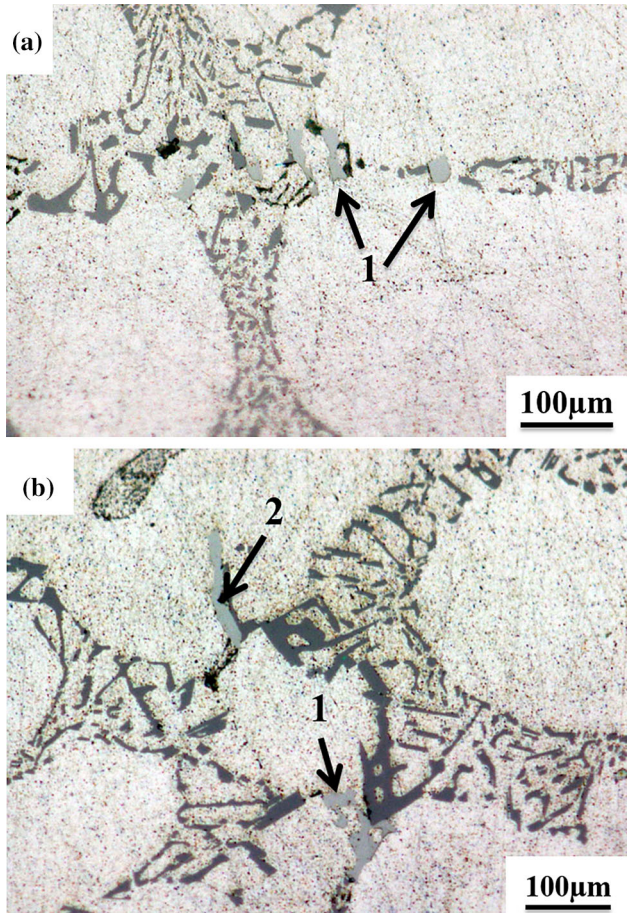

Fig. 3 Optical micrographs showing the microstructure of the iron-bearing phases in the as-cast A357 alloys: (a) alloy A (Zr-free) and (b) alloy B (Zr-containing). The arrows indicate: (1) a nodular intermetallic compound and (2) an acicular Al-Si-Ti-Zr phase

the duration of artificial aging toward the T6 heat treatment condition causes the evolution of the distribution to rodlike β'-Mg_2Si precipitates, producing the maximum strengthening of the alloy (Ref 16, 17). Figure 5 shows bright-field TEM micrographs of alloys A and B (Zr-containing) aged at 160 °C for 12 h (T6 heat treatment condition). The image shows the formation of a large quantity of rodlike β'-Mg_2Si precipitates with lengths of 20 to 50 nm, distributed throughout the matrix. However, the fine dispersoids of metastable Al_3Zr precipitates are not found in alloy B (Zr-containing). The T6 heat treatment was not able to promote the formation of metastable Al_3Zr precipitates (Ref 18). Figure 6(a) shows a TEM image of the microstructure obtained for the T6 heat-treated alloy A after thermal exposure at 250 °C for 50 h. It can be seen that the most common precipitates are the platelike β-Mg_2Si phase. The main rod-shaped β'-Mg_2Si precipitates in the T6 heat-treated alloy A have grown into platelike β-Mg_2Si precipitates about 20-30 nm in width and 200 nm in length. The platelike β-Mg2Si precipitates are completely incoherent with the matrix, as shown in Fig. 6(b). This, combined with their relatively large size and coarse distribution, can reasonably be expected to result in a significant decline in the performance of the T6 heat-treated alloy A under thermal exposure. Moreover, there is a remarkable amount of nearly spherical Al_3Zr phases dispersed within the matrix of the T6 heat-treated alloy B (Zr-containing) as a result of the thermal exposure at 250 °C (Fig. 7a). The Al_3Zr precipitates in the T6 heat-treated alloy B (Zr-containing) under thermal exposure conditions exhibit the classic lobed strain-field diffraction contrast, which indicates that the spherical metastable Al_3Zr phases maintain their coherence within the matrix, as is evident in Fig. 7(b). It is believed that coherence strain caused by the high antiphase boundary energy and the fairly large lattice misfit of the Al_3Zr phases contributes to pin the moving grain boundaries and disturbs the movement of dislocations, thereby improving the performance of the A357 alloy with the added Zr. Clearly, the mechanical properties of the Zr-containing alloy B at high temperatures can be improved by the homogeneously distributed Al_3Zr phases.

3.3 Electrical Conductivity Measurement

The growth and coarsening of precipitates reduce the number of solute atoms in the matrix and release the strain fields around those precipitates, which results in a continuous increase in the electrical conductivity during the aging heat treatment (Ref 19, 20). The electrical conductivity of alloys A and B (Zr-containing) under as-quenched (C_q), T6 heat-treated (C_{T6}) and thermal exposure (C_{100}) conditions are listed in Table 3. The as-quenched alloy B (Zr-containing) exhibited a lower electrical conductivity than alloy A, which was attributed to the Zr atoms in the Al matrix. After the aging treatment, the

strengthening β'-Mg_2Si phases precipitated from the supersaturated Al matrix, decreasing the solubility of Si and Mg in the solid solution. This acted to reduce the concentration of point defects inside the Al matrix and enhance the overall conductivity, as shown in Table 3. The relative variation in the electrical conductivity between the T6 heat-treated and the as-quenched alloy can be defined by $(C_{T6} - C_q)/\ C_q \times 100\%$. Variations in the amount of strengthening precipitates could be determined from the percentage of change in the electrical conductivity. The percentage of change in electrical conductivity (1.05%) in alloy A is similar to the 1.03% obtained for alloy B (Zr-containing). This shows that the addition of Zr did not enhance the amount of metastable Mg_2Si precipitates under the T6 condition. In addition, the change in the relative electrical conductivity between the T6 heat-treated (C_{T6}) and thermal exposed (C_{100}) conditions, given by $[(C_{100} - C_{T6})/C_{T6}] \times 100\%$, for the Zr-containing alloy B, was high. There was a dramatic increase in the electrical conductivity of alloys A and B (Zr-containing) under thermal exposed conditions were used. This indicates that there was substantial precipitation of unseparated atoms in the two T6 heat-treated alloys from the supersaturated matrix after treatment with the thermal exposed process, which reduced the concentration of defects in the matrix. The increase in the conductivity was highest in alloy B (Zr-containing), which is believed to be caused not only by precipitation of the metastable Mg_2Si, but also by precipitation of the Al_3Zr phase. The results are also consistent with the TEM phenomenon discussed in the previous section.

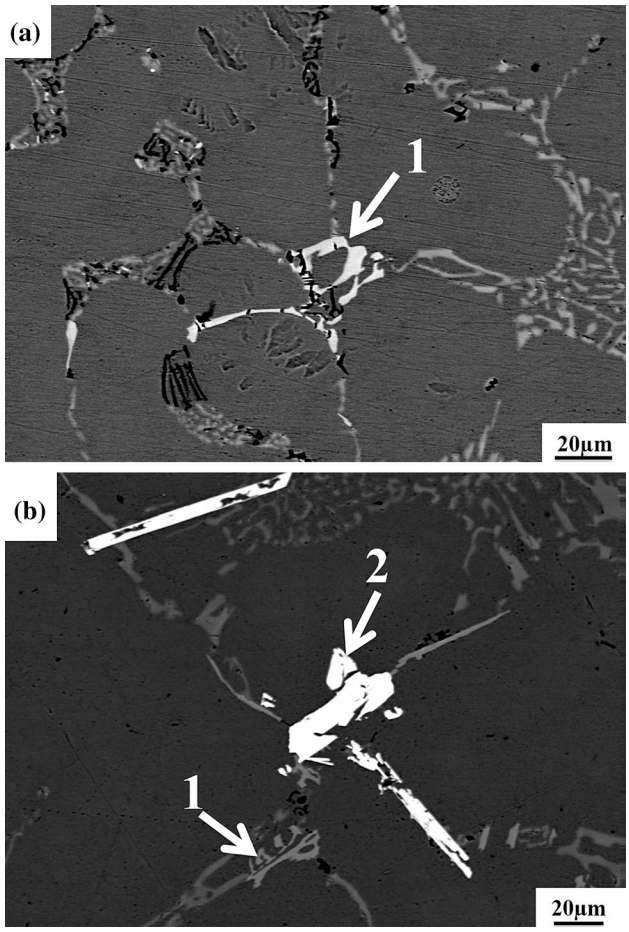

Fig. 4 Backscattered EPMA micrographs showing the morphology of iron-bearing phases in the as-cast A357 alloys with and without the addition of Zr: (a) alloy A (Zr-free) and (b) alloy B (Zr-containing). Note that numbered arrows corresponding to the iron-bearing phases as outlined in Table 2

3.4 Mechanical Properties

Figure 8 shows the evolution of the Rockwell hardness of the A357 alloys over time during artificial aging at 160 °C. As can be seen, under the as-quenched condition, the hardness of alloy B (Zr-containing) is superior to that of alloy A. This is because the addition of Zr to alloy B leads to a refining of the grain size of the Al matrix. Clearly, the addition of Zr has the effect of improving the hardness. In addition, the hardness of both alloys A and B (Zr-containing) increases rapidly with increased aging times, approaching peak values after approximately 5-10 h. The peak aging hardness increases after the addition of Zr to the A357 alloy. The results of tensile testing of A357 alloys under T6 condition are compiled in Table 4. The quality index (QI) provides a valuable tool for comparison of the relative advantage of the different alloys, combining the tensile strength and the elongation into a single parameter defined by QI = UTS + 150 × log elongation (for Al-7Si-Mg alloys) (Ref 21). It can be seen that alloy B (Zr-containing) exhibits higher tensile strength and quality index than alloy A. The excellent hardness and mechanical properties of alloy B (Zr-containing) can be attributed to the following reason: Although the addition of Zr does not bring prominent benefits in terms of the precipitation of strengthening Mg_2Si phases, it can help refine the grain size in the alloy. The significant reduction in the average grain size plays a crucial role in improving the performance of the A357 alloy. According to the Hall–Petch formula (Ref 22), the mechanical properties of T6 heat-treated alloy B (Zr-containing) are enhanced through the grain refining effect. Therefore, from Table 4, it can be observed that the ultimate tensile strength of T6 heat-treated alloy B (Zr-containing) increased from the 300 MPa of T6 heat-treated alloy A to 315 MPa. Due to the improved tensile strength, the quality index of T6 heat-treated alloy B (Zr-containing) was also higher than that of the T6 heat-treated alloy A.

Table 2 EPMA results for the intermetallic compounds marked by the white arrows and letters in Fig. 4 (wt.%)

Marked in Fig. 4	Shape	Phase	Modular formula	Al	Si	Fe	Mg	Zr	Ti
1	Nodular	Al-Si-Fe	$Al_7Si_2Fe_3$	63.5	9.1	27.2	N.D.	N.D.	N.D
2	Acicular	Al-Si-Ti-Zr	$(Al,Si)_3(Ti,Zr)$	30.9	27.1	N.D.	N.D.	21.8	19.8

N.D. not detectable

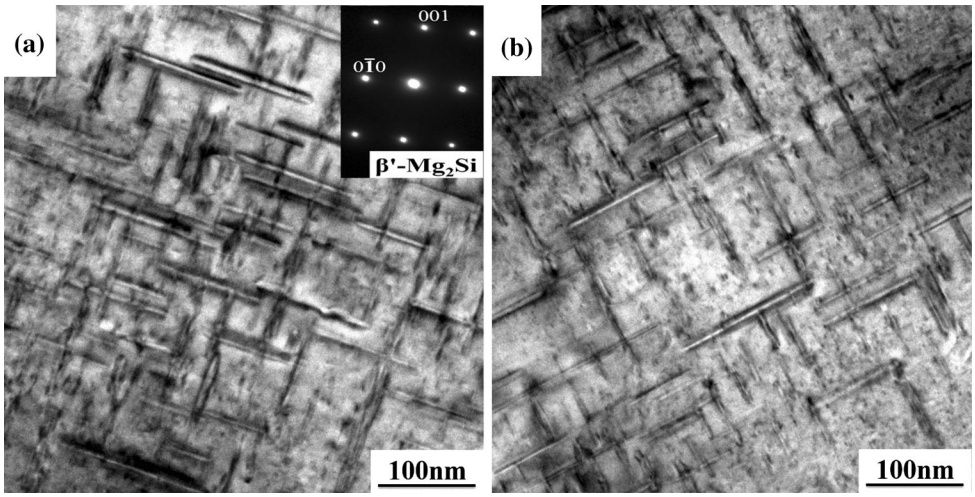

Fig. 5 TEM micrographs of the microstructure observed in the T6 heat-treated A357 alloy showing finely dispersed the β'-Mg_2Si precipitates throughout the Al matrix: (a) alloy A (the selected area diffraction pattern of the β'-Mg_2Si is inserted in the upper right corner) and (b) alloy B (Zr-containing)

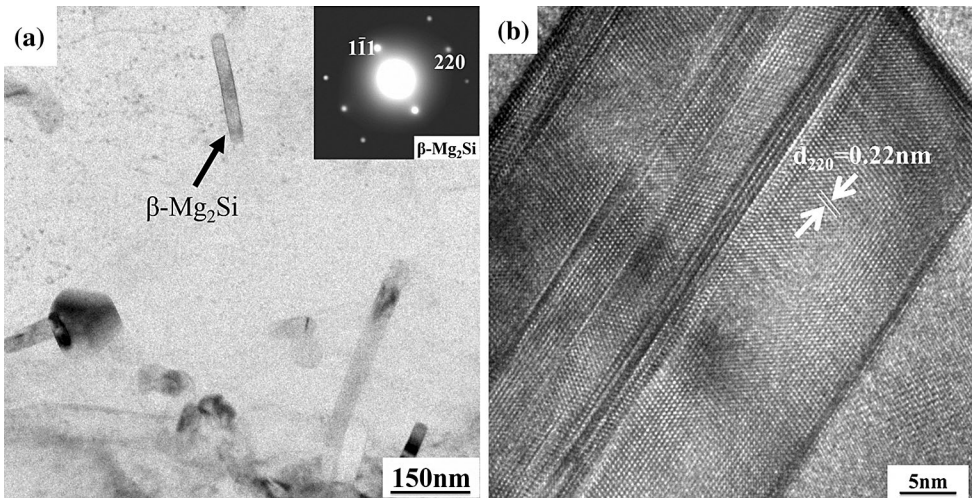

Fig. 6 TEM micrographs for the T6 heat-treated alloy A after thermal exposure at 250 °C for 50 h: (a) coarse equilibrium β-Mg_2Si precipitates distributed throughout the matrix (the selected area diffraction pattern of the β-Mg_2Si is inserted in the upper right corner) and (b) high-resolution TEM image of incoherent β-Mg_2Si phase

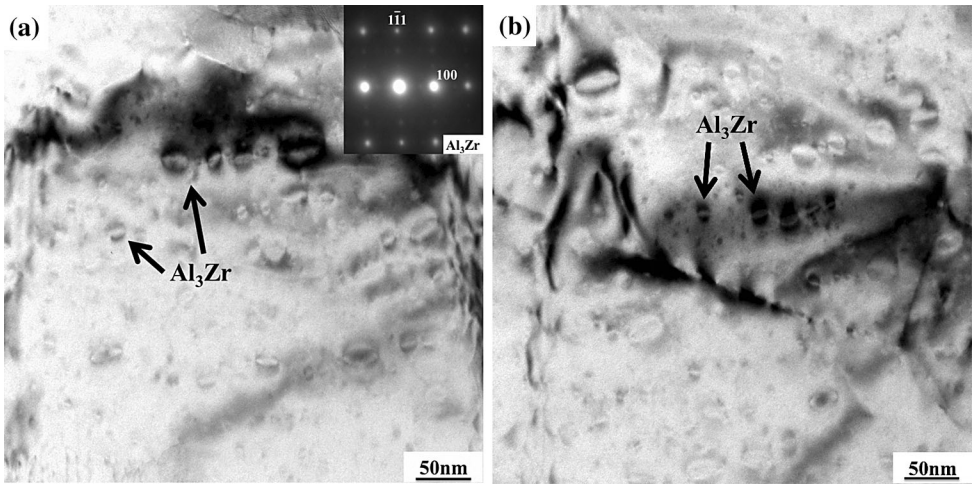

Fig. 7 TEM micrographs for the T6 heat-treated alloy B (Zr-containing) after thermal exposure at 250 °C for 50 h: (a) Al_3Zr precipitates (the selected area diffraction pattern of the Al_3Zr is inserted in the upper right corner) and (b) Al_3Zr precipitates with the classic lobed strain-field diffraction contrast

Table 3 Electrical conductivity (% IACS) of the A357 alloys under as-quenched, T6 heat-treated and thermal exposed conditions

Alloys	C_0	C_{T6}	C_{100}	$(C_{T6} - C_0)/C_0 \times 100\%$	$(C_{100} - C_{T6})/C_{T6} \times 100\%$
A	35.86 (0.02)	36.24 (0.04)	45.89 (0.03)	1.05%	26.62%
B(0.1Zr)	35.68 (0.03)	36.05 (0.02)	47.92 (0.02)	1.03%	32.92%

Standard deviations are listed in parenthesis

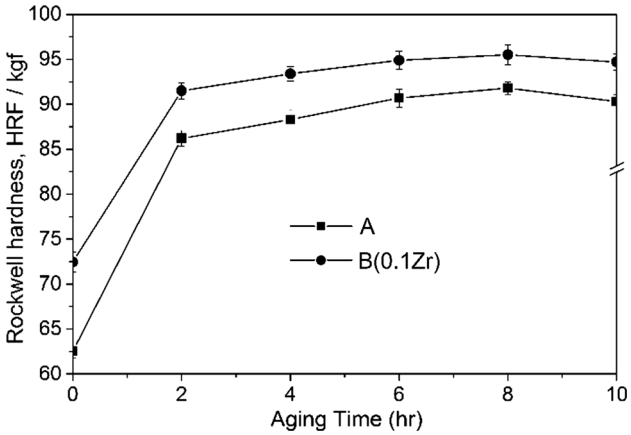

Fig. 8 Changes in the Rockwell hardness of alloys A and B (Zr-containing) with time during artificial aging at 160 °C

Table 4 Tensile properties of T6 heat-treated alloys A and B (Zr-containing)

	Properties			
Alloys	YS, MPa	UTS, MPa	EL., %	Q, MPa
A	248 (5)	299 (5)	3.8 (0.8)	385
B (0.1 Zr)	249 (4)	315 (5)	4.1 (0.5)	407

Standard deviations are listed in parentheses

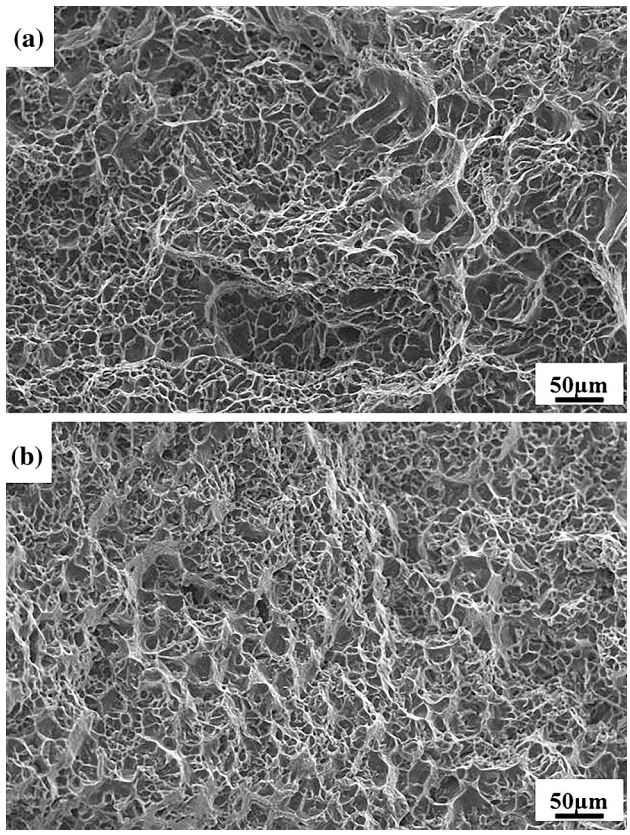

Fig. 9 The fracture micrographs of A357 alloys under T6 condition: (a) alloy A and (b) alloy B (Zr-containing)

Figure 9 shows the fracture images of the T6 heat-treated A357 alloys. The surfaces of T6 heat-treated alloys A and B (Zr-containing) contained a distribution of dimples. For T6 heat-treated alloy A, in Fig. 9(a), the dimples were coarser with noticeable cleavage planes. On the fractured surface of T6 heat-treated alloy B (Zr-containing), a relatively finer dimple distribution was observed, as depicted in Fig. 9(b). The dimple structures observed in the fractured surface of alloy A are much larger in size than those of alloy B (Zr-containing). This is expected, because of the larger grain size of alloy A than alloy B (Zr-containing).

3.5 Thermal Stability

The hardness and tensile properties of alloys A and B (Zr-containing) after thermal exposure at 250 °C for up to 100 h and after T6 heat-treated are plotted in Fig. 10. After thermal exposure at 250 °C for 100 h, there was degradation in the mechanical properties of both alloys A and B (Zr-containing). As mentioned above, after thermal exposure, all the finely dispersed β'-Mg2Si precipitates of the T6-treated alloy A and alloy B (Zr-containing) had grown into rod-shaped β-Mg2Si precipitates (as shown in Fig. 6). This change prompted the decline in the performance. However, it is obvious that the hardness and tensile properties of the Zr-containing alloy B remained significantly better than that of alloy A under thermal exposure conditions. This can be attributed to the precipitation of the coherent Al_3Zr phases. Therefore, it is very clear that the addition of Zr to the A357 alloys increases the hardness and tensile strength at high temperatures of up to 250 °C, leading to a higher heat resistance than would be possible for A357 alloys without Zr.

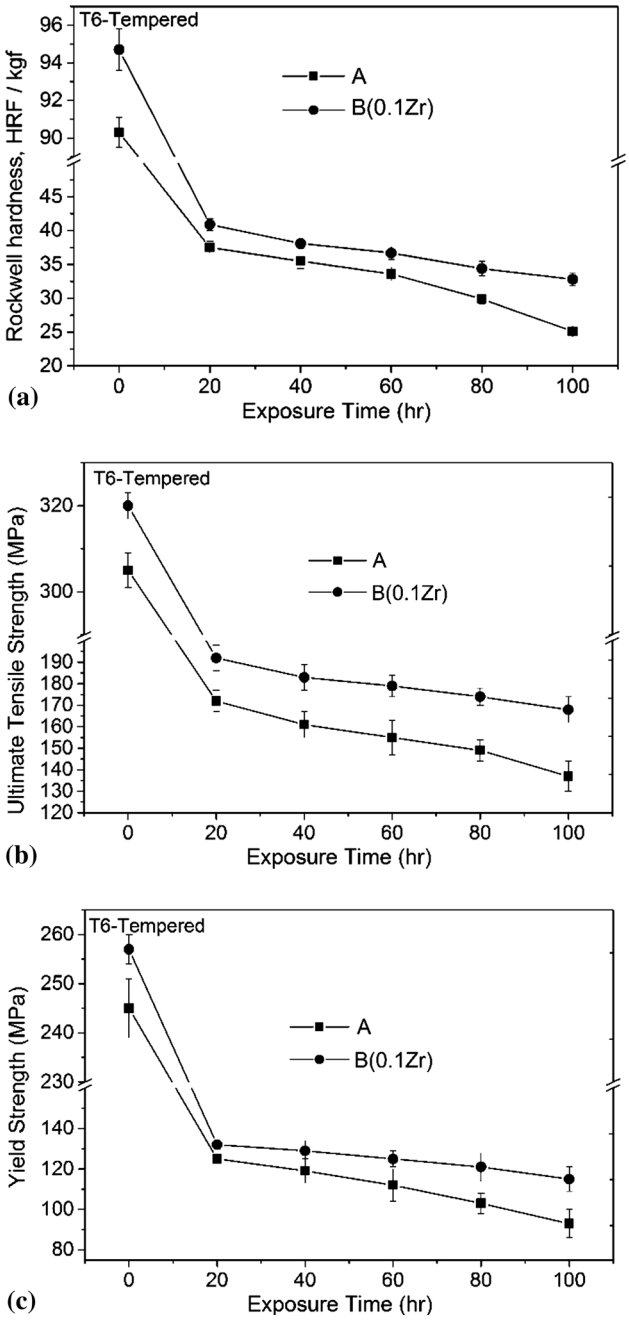

Fig. 10 Mechanical properties of the T6 heat-treated alloys A and B (Zr-containing) after thermal exposure at 250 °C for various times: (a) hardness; (b) ultimate tensile strength; and (c) yield strength

4. Conclusions

Based on the investigation of the correlation between the microstructure and mechanical properties of the A357 alloy with and without the addition of Zr, the experimental results support the following conclusions:

1. The iron-bearing phase of the Zr-free A357 alloy appeared as the $Al_7Si_2Fe_3$ phase; the iron-bearing phases in the Zr-containing A357 alloy were not only a $Al_7Si_2Fe_3$ phase but also a $(Al,Si)_3(Ti,Zr)$ phase.
2. The addition of 0.1% Zr did not affect the formation of finely dispersed Al_3Zr precipitates under the T6 heat-treated condition, but it did lead to grain refinement strengthening which played an important role in improving the hardness and tensile strength of the T6 heat-treated A357 alloys.
3. Thermal exposure induced the transformation of the metastable β'-Mg_2Si phases into the equilibrium β-Mg_2Si phases, resulting in a sharp decrease in the hardness and tensile strength of the T6 heat-treated A357 alloy without the Zr addition.
4. The addition of Zr prompted the formation of fine Al_3Zr precipitates during the thermal exposure process, effectively increasing the high-temperature performance of the A357 alloy.

Acknowledgments

The authors gratefully acknowledge the financial support received from the National Chung-Shan Institute of Science and Technology under Contract No. NCSIST-1164-V102 (106).

References

1. H. Ye, An Overview of the Development of Al-Si-Alloy Based Material for Engine Applications, *J. Mater. Eng. Perform.*, 2003, **12**, p 288–297
2. A.A. Canales, J.T. Silva, D. Gloria, S. Valtierra, and R. Colás, Thermal Analysis During Solidification of Cast Al-Si Alloys, *Thermochim Acta*, 2010, **510**, p 82–87
3. Y.H. Tan, S.L. Lee, and Y.L. Lin, Effects of Be and Fe Content on Plane Strain Fracture Toughness in A357 Alloys, *Metall. Mater. Trans. A*, 1995, **26**, p 2937–2945
4. Y.H. Tan, S.L. Lee, and Y.L. Lin, Effects of Be and Fe Additions on the Microstructure and Mechanical Properties of A357.0 Alloys, *Metall. Mater. Trans. A*, 1995, **26**, p 1195–1205
5. A.M. Samuel, H.W. Doty, S. Valtierra, and F.H. Samuel, Relationship between Tensile and Impact Properties in Al-Si-Cu-Mg Cast Alloys and Their Fracture Mechanisms, *Mater. Des.*, 2014, **53**, p 938–946
6. T. Gao, X. Zhu, Q. Sun, and X. Liu, Morphological Evolution of ZrAlSi Phase and its Impact on the Elevated-temperature Properties of Al-Si Piston Alloy, *J. Alloys Compd.*, 2013, **567**, p 82–88
7. R. Mahmudi, P. Sepehrband, and H.M. Ghasemi, Improved Properties of A319 Aluminum Casting Alloy Modified with Zr, *Mater. Lett.*, 2006, **60**, p 2606–2610
8. M.F. Ibrahim, E. Samuel, A.M. Samuel, A.M.A.A. Ahmari, and F.H. Samuel, Impact Toughness and Fractography of Al-Si-Cu-Mg Base Alloys, *Mater. Des.*, 2011, **32**, p 3900–3910
9. C. Shi and X.G. Chen, Hot Workability and Processing Maps of 7150 Aluminum Alloys with Zr and V Additions, *J. Mater. Eng. Perform.*, 2015, **24**, p 2126–2139
10. J.D. Robson and P.B. Prangnell, Dispersoid Precipitation and Process Modelling in Zirconium Containing Commercial Aluminium Alloys, *Acta Mater.*, 2001, **49**, p 599–613
11. Y.V. Milman, A.I. Sirko, D.V. Lotsko, D.B. Miracle, and O.N. Senkov, Microstructure and Mechanical Properties of Cast and Wrought Al-Zn-Mg-Cu Alloys Modified with Zr and Sc, *Mater. Sci. Forum*, 2002, **396–402**, p 1217–1222
12. B. Morere, R. Shahani, C. Maurice, and J. Driver, The Influence of Al_3Zr Dispersoids on the Recrystallization of Hot-Deformed AA 7010 Alloys, *Metall. Mater. Trans. A*, 2001, **32**, p 625–632
13. B. Baradarani and R. Raiszadeh, Precipitation Hardening of Cast Zr-containing A356 Aluminium Alloy, *Mater. Des.*, 2011, **32**, p 935–940
14. TRIMET Aluminium SE: Product-Information Trimal-37 (1/2016)
15. J. Hernandez-Sandoval, G.H.G. Elizondo, A.M. Samuel, S. Valtiierra, and F.H. Samuel, The Ambient and High Temperature Deformation Behavior of Al-Si-Cu-Mg Alloy with Minor Ti, Zr, Ni Additions, *Mater. Des.*, 2014, **58**, p 89–101

16. E. Sjolander and S. Seifeddine, The Heat Treatment of Al-Si-Cu-Mg Casting Alloys, *J. Mater. Process. Technol.*, 2010, **210**, p 1249–1259
17. G. Edwards, K. Stiller, G. Dunlop, and M. Couper, The Precipitation Sequence in Al-Mg-Si Alloys, *Acta Mater.*, 1998, **46**(11), p 3893–3904
18. K.E. Knipling, D.C. Dunand, and D.N. Seidman, Precipitation Evolution in Al-Zr and Al-Zr-Ti Alloys During Isothermal Aging at 375–425 °C, *Acta Mater.*, 2008, **56**(1), p 114–127
19. S.F. Fang, M.P. Wang, and M. Song, An Approach for the Aging Process Optimization of Al-Zn-Mg-Cu Series Alloys, *Mater. Des.*, 2009, **30**, p 2460–2467
20. C.T. Wu, S.L. Lee, M.H. Hsieh, and J.C. Lin, Effects of Cu content on Microstructure and Mechanical Properties of Al-14.5Si-0.5Mg Alloy, *Mater. Charact.*, 2010, **61**, p 1074–1079
21. M. Drouzy, S. Jacob, and M. Richard, Interpretation of Tensile Results by Means of Quality Index and Probable Yield Strength, *AFS Int. Cast Metal.*, 1980, **5**, p 43–50
22. Y. Haiyang, Y. Hongge, C. Jihua, S. Bin, Z. Yi, S. Yanjin, and M. Zhaojie, Effects of Minor Gd Addition on Microstructures and Mechanical Properties of the High Strain-Rate Rolled Mg-Zn-Zr alloys, *J. Alloys Comp.*, 2014, **586**, p 757–765